




Anisotropic Mechanical Properties of the Human Uterus Measured by Spherical Indentation

SHUYANG FANG,¹ JAMES MCLEAN,² LEI SHI,¹ JOY-SARAH Y. VINK,³
CHRISTINE P. HENDON,² and KRISTIN M. MYERS¹ 

¹Department of Mechanical Engineering, Columbia University, New York, NY 10027, USA; ²Department of Electrical Engineering, Columbia University, New York, NY 10027, USA; and ³Department of Obstetrics and Gynecology, Columbia University Irving Medical Center, New York, NY 10032, USA

(Received 2 November 2020; accepted 26 March 2021; published online 20 April 2021)

Associate Editor Raffaella De Vita oversaw the review of this article.

Abstract—The mechanical function of the uterus is critical for a successful pregnancy. During gestation, uterine tissue grows and stretches to many times its size to accommodate the growing fetus, and it is hypothesized the magnitude of uterine tissue stretch triggers the onset of contractions. To establish rigorous mechanical testing protocols for the human uterus in hopes of predicting tissue stretch during pregnancy, this study measures the anisotropic mechanical properties of the human uterus using optical coherence tomography (OCT), instrumented spherical indentation, and video extensometry. In this work, we perform spherical indentation and digital image correlation to obtain the tissue's force and deformation response to a ramp-hold loading regimen. We translate previously reported fiber architecture, measured via optical coherence tomography, into a constitutive fiber composite material model to describe the equilibrium material behavior during indentation. We use an inverse finite element method integrated with a genetic algorithm (GA) to fit the material model to our experimental data. We report the mechanical properties of human uterine specimens taken across different anatomical locations and layers from one non-pregnant (NP) and one pregnant (PG) patient; both patients had pathological uterine tissue. Compared to NP uterine tissue, PG tissue has a more dispersed fiber distribution and equivalent stiffness material parameters. In both PG and NP uterine tissue, the mechanical properties differ significantly between anatomical locations.

Keywords—Biomechanics, Human uterus, Anisotropy, Inverse finite element analysis.

INTRODUCTION

The human uterus is a pear-shaped, thick-walled, smooth muscle-rich organ within which the fetus develops during pregnancy. Throughout gestation, the uterine wall (myometrium) remains in a passive state and accommodates the expanding amniotic sac by growing, unfolding, and stretching. Then, ideally at term (defined as 37 weeks), the onset of labor triggers a drastic functional change in the uterus: its tissue becomes highly excitable and contractile to safely deliver the baby.^{41,51} Early contractile activation of uterine tissue can lead to preterm labor and birth (PTB).⁹ In 2015, more than 10 percent of pregnancies around the globe ended in PTB; PTB is also the leading cause of death in children under five years of age.³³ In addition, medically necessary induction of labor past term via Cesarean section is likewise associated with its own set of risks.^{3,14} The mechanical function of uterine tissue is critical for a healthy pregnancy and safe delivery, yet little is known about its material properties and its mechanical response during pregnancy. Therefore, characterizing uterine mechanical properties is essential for understanding the mechanisms of its mechanical failure and causes of PTB.

Previous studies using magnetic resonance imaging (MRI) have discovered the human uterus is a fibrous tissue exhibiting significant anisotropy across different anatomical regions and throughout the depth of the uterine wall.^{47,60} Studies on other fibrous biological tissues have found the distributions of its constituent fibers have a significant impact on its stress and deformation response to different loading regimes.²⁵

Address correspondence to Kristin M. Myers, Department of Mechanical Engineering, Columbia University, New York, NY 10027, USA. Electronic mail: kmm2233@columbia.edu

Hence, uncovering the structure of a tissue's fiber network is critical to understanding its mechanical properties.

Advanced imaging modalities and mechanical testing frameworks have been successful at measuring the anisotropic material properties of soft collagenous tissues. Previous studies have used optical coherence tomography (OCT) to investigate cervical collagen ultrastructure for cancer detection^{32,44} and to map human cervical collagen fiber architecture at different anatomical locations.^{17,62} Instrumented indentation, coupled with video extensometry, is a non-destructive mechanical testing modality that can explore the anisotropic mechanical properties of fibrous materials. A previous study had used a four-step incremental indentation test on tissue-equivalents to investigate their fibrillar organization.³¹ Another study on human cervical tissue has combined indentation testing with inverse finite element analysis (IFEA) to characterize its anisotropic mechanical properties.⁵⁰ Building off of these previous investigations, the goal of this study is to use these methods (OCT, indentation testing, and IFEA) to characterize the anisotropic mechanical properties of the human uterus. Given the constraints on the availability of human uterine tissue samples, we report only observed material properties for uterine tissue taken from hysterectomy patients with reported uterine and/or placental pathologies.

MATERIALS AND METHODS

Specimen Collection and Preparation

Uterine specimens were collected from two patients: one non-pregnant (NP), premenopausal patient (< 50 years old) who underwent a total hysterectomy due to a benign indication and another pregnant (PG) patient who underwent a Cesarean section hysterectomy due to abnormal placentation at 34 weeks gestation. This study was approved by the institutional review boards at the medical center of Columbia University, and each subject provided written informed consent. Patients' demographic data are listed in Table 1.

Immediately after hysterectomy, a specimen was collected from each of three uterine anatomical loca-

tions: the mid-anterior (front wall of the uterus), the posterior (back wall of the uterus), and the fundus (the top of the uterus) (Figs. 1(a) and 1(b)). All specimens were full-thickness samples ranging from 15 to 35 mm in depth and covered a square cross-sectional area with an edge between 15 and 25 mm. All specimens were flash-frozen using dry ice immediately after collection and then stored in a -80°C freezer (Thermo Fisher Scientific Inc., Waltham, MA) prior to OCT scanning or mechanical testing.

Before each OCT scan or mechanical test, the specimens were thawed and equilibrated at 4°C for 12 hours using phosphate-buffered saline (PBS) solution. We performed a swelling test similar to our previous study to determine this thawing protocol.²⁷ Then, each specimen was cut into four to eight slices parallel to the uterine wall using a customized slicer to ensure each slice's smoothness. The slice dimensions of the NP and PG specimens are listed in Table 2. The slices were numbered from the outermost layer to the innermost layer with increasing numbers starting from 1 (Fig. 1(c)).

Optical Coherence Tomography

To investigate the fibrous network architecture, three-dimensional volumetric image-sets were obtained from human uterine specimens using a commercial spectral-domain OCT system, TELESTO (Thorlabs GmbH, Germany), with $6.5\ \mu\text{m}$ axial resolution, $15\ \mu\text{m}$ lateral resolution, and 2.51 mm imaging depth, in air. To avoid specimen movement, each slice was laid on top of a coarse cork taped to a weighing boat. The top of the specimen slice was dried to avoid reflection, while the bottom was submerged into PBS to keep the tissue hydrated. The weighing boat was placed on a linear translation stage underneath the objective lens. For each slice, both sides were imaged with multiple volumes obtained by moving the stage horizontally along the x- or y-axis. Since the surface of the slice was not completely flat, the z-axis position of the slice was also adjusted vertically to obtain best-focused images. Each volume consisted of $1375 \times 1375 \times 512$ voxels, corresponding to a tissue

TABLE 1. Patient specific obstetric history.

Patient	Age	Ethnicity	G	P	HYST indication	Obstetric history
NP	40	AA	0	0	Symptomatic uterine fibroids	No pregnancies
PG	39	White	11	2	34 weeks gestation; complete previa; suspected placenta accreta	Prior C/S \times 2

G \equiv Gravida; P \equiv Parity; HYST \equiv hysterectomy; NP \equiv Non-pregnant; AA \equiv African-American; PG \equiv Pregnant; C/S \equiv Cesarean section.

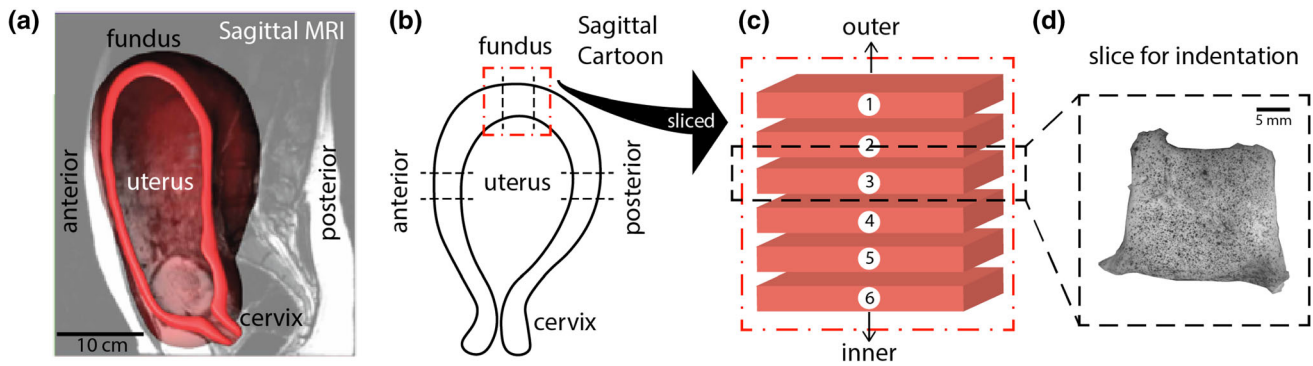


FIGURE 1. Human anatomy, tissue collection, and specimen preparation. (a) The uterus and cervix are segmented from an MRI of a 24-week pregnant patient.¹² (b) Uterine specimens were collected through the full thickness at three anatomical locations: the anterior (front) wall, the posterior (back) wall, and the fundus (top). (c) Each specimen was sliced through the thickness, parallel to the uterine wall surface, into multiple slices with a height of 3 to 5 mm. The tissue slices were numbered 1 to 6 from the outermost to the innermost layer. (d) A representative specimen slice viewed from the bottom (with speckling pattern for digital image correlation analysis (“Digital Image Correlation (DIC)” section)).

TABLE 2. Uterine specimen dimensions.

Tissue type	Length (mm)	Width (mm)	Thickness (mm)
NP	23.07±2.40	20.41±2.91	4.84±0.61
PG	25.30±3.21	20.82±3.70	4.43±0.93

volume of $5.5 \times 5.5 \times 2.51 \text{ mm}^3$. A 10% scanning overlap was applied between adjacent volumes for image stitching. A white-light camera image was obtained simultaneously with an OCT image to delineate the field of view of the tissue. All volumes were stitched adjacently to create a single mosaic volume using the image blending algorithm developed in a previous study.¹⁷

Masson trichrome stained histology was applied to eight of the slices (2 NP & 6 PG) to evaluate the microscopic tissue structure and to later compare with OCT results (Fig. 2).¹⁵ By Masson trichrome protocol, collagen and muscle tissue were stained blue and red, respectively (Fig. 2(a)). In an OCT image, the extracellular matrix (ECM) presents as a higher-intensity region when compared with muscle tissue (Fig. 2(b)). Biologically, collagen fibers are ECM components and act as a sheath separating, structurally supporting, and aligned with muscle fiber bundles.^{48,58} Consequently, we characterized the fibrous network orientation by tracking the orientation of the collagen fibers. Note that, given the resolution of the OCT image, the term “fiber” here technically describes a fiber bundle, which typically comprises hundreds of fibers that align in the same direction. In this study, we measured network characteristics at the scale of a fiber bundle ($>10 \mu\text{m}$).^{5,13,34} Hence, throughout the manuscript, fiber alignment and dispersion describe the characteristics of a fiber bundle as delineated in the OCT. The 3-

D collagen fiber architecture was mapped for each OCT mosaic volume using a previously developed custom image processing pipeline.³⁸ The OCT images were first de-noised and processed to enhance the collagen fiber contrast. Valid regions of fiber measurement were determined by segmenting the uneven tissue surface using edge detection. The 3-D collagen fiber *en-face* orientation is measured at each image voxel and is described by the in-plane orientation map $\theta(x, y, z)$, whose value of zero starts at the positive x-axis. A local gradient-based method was applied to each *en-face* OCT image of the mosaic volume to obtain $\theta(x, y, z)$.¹³ The gradient method operated within a small “window” of the image and then calculated the fiber orientation within the windowed area. Local orientation was determined by the direction along which the image gradient was maximized within each window. The image gradient was obtained using 2-D, 3×3 pixel, horizontal and vertical Sobel filters G_x and G_y , and the gradient direction was $\theta' = \arctan(G_y/G_x)$. A D’Agostino-Pearson κ^2 (normality) test was used to determine if a windowed image area contained a valid fiber orientation.² A κ^2 threshold value of 0.02 and a window size of 51×51 pixels was selected for all analyses.

Fiber Distribution Characterization

We used a von Mises distribution to characterize the fiber distribution in the uterine samples, where we focus the characterization at a region of interest (ROI) centered under the indenter. The von Mises distribution is commonly used to characterize fibers in soft biological tissues when preferential fiber direction and fiber dispersion significantly impact the tissues’ stress and deformation under different loading regimes.^{18,25}

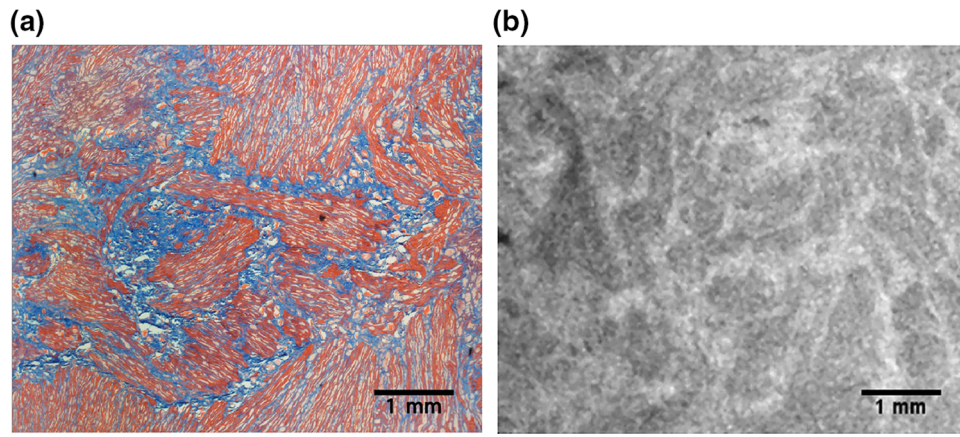


FIGURE 2. OCT and histology to verify tissue composition in the NP uterus. (a) Masson trichrome stained histology section from the NP anterior uterine wall. The blue stain represents collagen, and the red stain represents smooth muscle tissue. (b) OCT *en-face* image from the same uterine tissue sample. Features are not matching exactly due to the small scale and different view depths of the images. The visual comparison shows that in the OCT image, the higher intensity areas are collagen fibers, while the lower intensity areas between collagen fibers are smooth muscle tissue.

A typical von Mises, also known as the circular normal distribution, is defined continuously over the range, in radians, from zero to 2π . Fibers, however, have orientations rather than directions; as such, they span the range, in radians, from zero to π . Therefore, a hybrid method was developed in this study to characterize the fiber distribution by fitting a π -periodic von Mises distribution, or a mixture of them, to the θ values determined from OCT (“[Optical Coherence Tomography](#)” section). To incorporate the OCT results into our IFEA workflow and to balance computational cost with accuracy, we selected a region in the tissue with the largest strains and an approximately uniform stress distribution as the ROI. This 2-mm diameter circle centered at the specimen bottom is informed by our preliminary FEA results (not shown here). The number of distributions was iteratively tested to find the best fit. The modified probability density function for a single π -periodic von Mises is defined, following a previous study,⁵⁹ as:

$$f(x|\mu, \kappa) = \frac{1}{\pi} \frac{e^{\kappa \cos(2(x-\mu))}}{I^0(\kappa)} \quad (1)$$

where μ is a measure of mean angle, representing the preferred fiber orientation; κ is a measure of concentration (a reciprocal measure of dispersion), with small κ representing a close-to uniform (very dispersed) distribution and large κ representing a distribution very concentrated around the angle μ ; and I^0 is the modified Bessel function of order zero. We calculated μ using an R package, BAMBI (BAMBI only supports estimation of parameters for a 2π -periodic von Mises distribution. However, the relationship between θ and μ is stable under linear transformation. Therefore, we fitted the distribution to raw θ values multiplied by

two. The recovered μ was then divided by two to return its π -periodic value).⁷ κ was calculated using a root-finding algorithm in R to solve for the equation

$$n \frac{I^1(\kappa)}{I^0(\kappa)} - \sum_{i=1}^n \cos(2(x - \mu)) = 0, \kappa > 0 \quad (2)$$

where I^0 and I^1 are the modified Bessel functions of orders zero and one, and n is the size of θ .

Indentation Test Regimen

A four-level, ramp-hold indentation test was performed using a customized experiment rig (Fig. 3(a)). To keep the specimen slice hydrated throughout the test and to allow tracking of its speckled bottom surface for DIC analysis (“[Digital Image Correlation \(DIC\)](#)” section), we placed the specimen in a PBS-filled bath chamber with a clear acrylic window on the bottom. Below the window, a 90° prism was fixed to reflect the specimen bottom into a charge-coupled device camera (Point Gray Grasshopper, GRAS-50S5M-C75 mm, $f/4$ lens) at the front. The light was cast by two LYKOS Daylight LED lights (Vitec Imaging Distribution Inc, Upper Saddle River, NJ) from the front. We placed the experiment rig on a universal testing machine (Instron, Inc., Norwood, MA). Indentation tests were performed using a 6-mm diameter spherical indenter attached to a 5 N load cell (Instron, Inc., Norwood, MA, accuracy of 0.005 N).

To find the zero-contact point before each test, the indenter was positioned closely above the specimen and moved down in $8 \mu\text{m}$ increments until a force change greater than 0.15 mN was observed. The indenter was then moved out of contact with the specimen, and the specimen was allowed to equilibrate

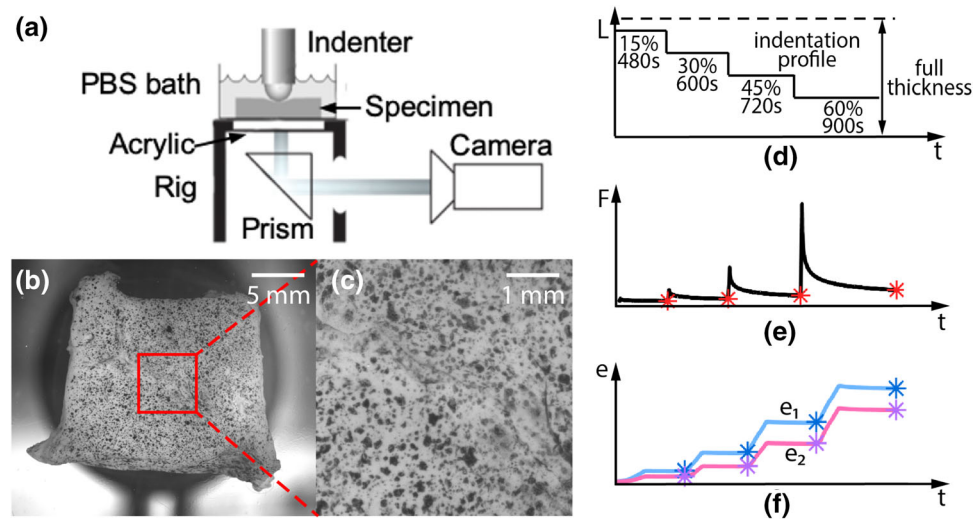


FIGURE 3. Indentation test setup, test protocol profile, and corresponding force and strain data (a) Schematic illustration of the custom indentation test rig. The clear acrylic window allows the front camera to capture the deformation of the specimen bottom surface. (b) A representative image of the specimen bottom surface and its speckle pattern. The indentation test was performed at the center of the red square shown by (c). (d) A four-level ramp-hold protocol was used for the indentation test. The indentation depth was prescribed as a percentage of the full tissue thickness at the indenting location. The tissue was held for a sufficient time to equilibrate after each displacement. (e) The force–time data of the indenter are shown as a black line, with asterisks marking the equilibrium state at each level. (f) First (e_1) and second (e_2) principal strain of the specimen bottom under the indenter are shown as the continuous lines, with asterisks marking the equilibrium state at each level.

for one minute. The force was reset before the actual test. Indentation depths were prescribed as displacement—15, 30, 45, and 60% of the specimen thickness at the indenting location (Fig. 3(d)). To avoid horizontal movement during testing, all the specimen slices were indented in the center. (A small number of slices were indented slightly off-center due to the speckle quality and smoothness of their bottom surfaces.) For all the slices, the ramping rate was one percent of the thickness per second. After each ramp, the indenter was held still for 480, 600, 720, and 900 seconds, respectively, for the specimen tissue to relax and reach an equilibrium. Force–time (N·s) data were recorded using a material tester software (Instron, Inc., Blue Hill version 3.11.1209) (Fig. 3(e)).

Digital Image Correlation (DIC)

DIC, a non-contact, length scale-independent technique, was used to measure displacements and calculate the 2-D strain field of the specimen's bottom surface.⁵³ The correlation algorithm identifies unique pattern features within multiple small pixel subsets. It tracks the translation, rotation, and deformation of each subset, rendering the full-field displacements and corresponding strains. 2-D DIC was applied in this scenario of planar test subjects. Before indentation tests, each specimen slice was dried and speckled with Verhoeff's elastic stain (VEG). Black water-insoluble ink (Chartpak, Inc., Leeds, MA) was applied to the bottom surface using an

airbrush (Harder & Steenbeck GmbH & Co., Germany) and a Sprint Jet air compressor (Iwata Medea Inc., Portland, OR) (Fig. 3(b)). The camera aperture was set to produce a high contrast while maximizing the depth of field. Images were taken using Vic-Snap (Correlation Solutions, v2010, Irmo, SC) at two set acquisition rates: two images per second during the ramps and one image every 30 seconds during the holds. Calibration images were taken for each test set; a ruler with 1/16 inch gradations was included in the field of view.

The images were processed using software Vic-2D (Correlated Solutions, v6) with an incremental correlation method where a seed point was defined in one image and searched in the following ones. A square area with discernible displacement and good speckle quality was selected around the indentation center to perform a good correlation. The correlation quality is indicated by the confidence interval σ , a parameter calculated by the DIC software to show the match at this point, in pixels.⁵² A confidence interval larger than 95% was set to determine a good correlation. The area of interest was then meshed into square subsets with an edge between 47 and 61 pixels (0.69–0.90 in mm), where each subset had a unique speckle pattern to improve tracking. Step size, the spacing of pixels between each analysis step during correlation, was set to be roughly 1/4 of the subset size as suggested by the software manual. The displacement field was converted from the pixel field to mm using the calibration images. The first and second principal Lagrangian strains (e_1^{DIC}

and e_2^{DIC}) were calculated using a 90% centered Gaussian filter (Fig. 3(f)).

Finite Element Analysis (FEA)

FEA was performed to simulate and compare with the mechanical tests using FEBio Software Suite (Salt Lake City, Utah). The actual length, width, and thickness of the specimen slice were measured after thawing to create the computational model. Finite element models were created in Preview, the preprocessor of FEBio specifically designed for setting up FE problems. A rectangular cuboid represented the specimen slice, and a 6-mm diameter rigid sphere represented the stainless steel indenter. The solid model of the uterine slice and the indenter sphere were both meshed using HEX-8 elements, which are computationally cheaper with satisfactory accuracy for simple geometries compared to TET-10 elements.⁵⁴ A mesh convergence study (not detailed here) showed an adequate discretization with an element edge length of 0.5 mm. The number of elements ranged from 11,648 to 18,048, depending on different specimens' sizes. We applied a sliding-tension-compression contact between the lower hemisphere of the indenter and the top surface of the specimen. This contact mode allows a surface to separate from the other or have contact and slide across the other (but not to penetrate), representing the frictionless interface between the indenter and the specimen in the experiments. Only the z-displacement (vertical) of the specimen bottom was fixed as it could not penetrate but could move freely across the bath chamber. These frictionless contact assumptions were guided by the fact we were interrogating equilibrium and quasi-static loading conditions. Previous studies on soft collagenous tissues have adopted this assumption.^{10,30,35,49,64} In addition, our friction sensitivity study, using finite element analysis, on both contact surfaces found less than 5% change in both indenter force and specimen bottom principal strains. A fixed-displacement boundary condition was applied to the specimen's further side to stabilize the geometry (Fig. 4(b)). The indentation profile was modeled as a prescribed displacement (“[Indentation Test Regimen](#)” section notices); the process was divided equally into four steps to model the four-level ramp-hold protocol. The rigid sphere (indenter) was placed on the cuboid (specimen) top surface at time point zero to simulate the zero-contact point in the mechanical test.

Constitutive Model

Uterine tissue in this study was modeled using a previously published constitutive material model,⁵⁰

where a continuously distributed 3-D fibrous network was embedded in a compressible neo-Hookean ground substance. This material model was verified for human cervical tissue, consisting mostly of collagen fibers embedded in an elastic ground substance. The human uterine tissue has the same framework but with smooth muscle fibers in addition to collagen fibers as the fibrous network. Biologically, uterine smooth muscle cells (SMCs) and collagen fibers have some degree of interconnectivity: SMCs are grouped into fiber bundles by connective tissue within and around the bundle. The connective tissue is predominantly composed of collagen. Mechanically, a previous study on the material properties of muscle fiber composites (muscle and collagen) showed its fiber modulus, a measurement of fiber stiffness, is about five times higher than that of muscle fiber alone, indicating collagen fibers acting as the primary load-bearing component.⁴ Consequently, collagen and smooth muscle fibers were altogether modeled as the fibrous network here. (This simplifying assumption is a limitation of the model. Once additional experimental evidence of the interconnectivity of the uterine collagen and SMCs are realized, the material model can be refined.) The total Helmholtz free energy density Ψ , therefore, is an additive contribution from a ground substance Ψ^{GS} of non-fibrous ECM components and the fibrous network Ψ^{FN} . This is expressed by

$$\Psi(\mathbf{F}, \mathbf{n}) = \Psi^{GS}(\mathbf{F}) + \Psi^{FN}(\mathbf{F}, \mathbf{n}) \quad (3)$$

where \mathbf{F} is the deformation tensor and \mathbf{n} is the preferential direction of the fiber distribution.

The strain-energy function for the neo-Hookean ground substance Ψ^{GS} and the fibrous network Ψ^{FN} are as follows, respectively,

$$\Psi^{GS} = \frac{\mu}{2}(I_1 - 3) - \mu \ln J + \frac{\lambda}{2}(\ln J)^2 \quad (4)$$

$$\Psi^{FN}(\mathbf{F}, \mathbf{n}) = \int_0^{2\pi} \int_0^\pi H(I_n - 1) \Psi_n^{FN}(I_n) \frac{1}{\pi} \sqrt{\frac{\kappa}{2\pi}} \frac{e^{2\kappa n^2}}{\text{erfi}(\sqrt{2\kappa})} \sin \phi \, d\phi \, d\theta \quad (5)$$

where μ (only here) and λ are Lamé parameters and can be converted to Young's modulus E and Poisson's ratio ν . κ is the von Mises concentration factor characterized in “[Fiber Distribution Characterization](#)” section. I_1 is the first invariant of right Cauchy-Green deformation tensor $\mathbf{C} = \mathbf{F}^T \mathbf{F}$, and $\mathbf{J} = \det \mathbf{F}$ is the determinant of the deformation gradient tensor. $H(\cdot)$ is the Heaviside unit step function that ensures fibers are only active in tension, since collagen fibers cannot support compressive stresses due to their wavy struc-

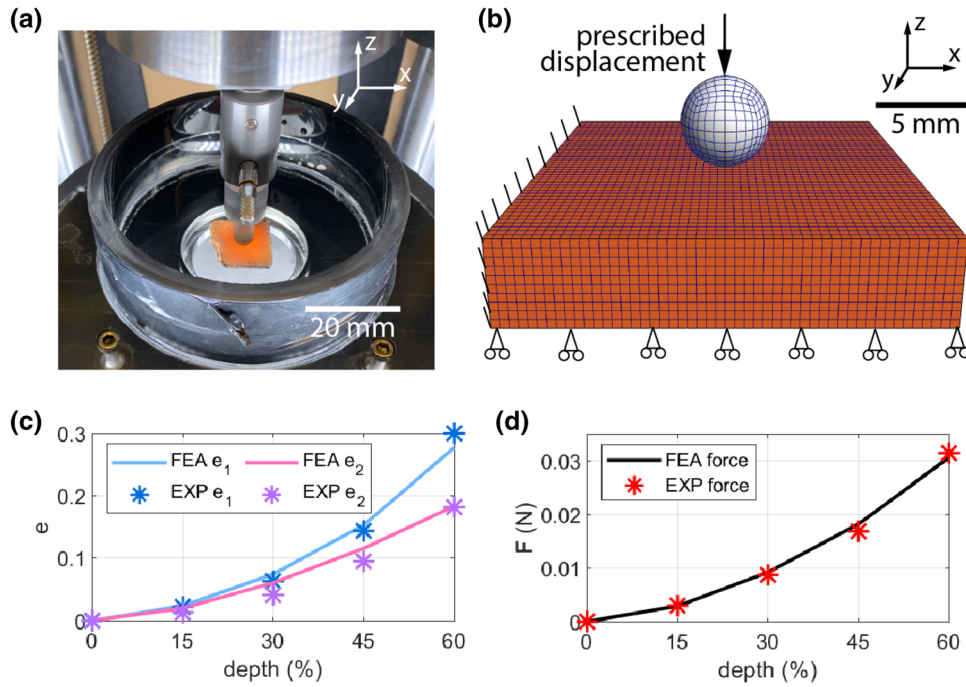


FIGURE 4. A finite element model was built to simulate the indentation test, and its strain and force responses were compared with the experimental data to find best-fit material parameters. (a) The indentation test was performed on the specimen slice in a PBS bath using the universal testing machine. (b) The specimen was modeled as a rectangular cuboid with its bottom surface restrained in the z-direction and one side restrained in all directions to stabilize the geometry. The indenter was modeled as a rigid sphere with a prescribed displacement in the z-direction. Both parts were meshed using HEX-8 elements. (c) The lines represent the first (e_1^{FEA}) and second (e_2^{FEA}) principal strain responses in FEA, while the asterisks represent the experimental equilibrium strain responses (e_1^{EXP} and e_2^{EXP}). (d) The line represents the FEA force response (F^{FEA}) while the asterisks represent the experimental equilibrium force responses (F^{EXP}).

ture.²⁴ $I_n = \mathbf{n} \cdot \mathbf{C} \cdot \mathbf{n}$ is the normal component of \mathbf{C} along \mathbf{n} . $erfi(\cdot)$ is the imaginary error function, and ϕ and θ (only here) are the spherical coordinates.

The exponential law gives the strain-energy density function of a single fiber

$$\Psi_n^{FN} = \frac{\xi}{2\alpha} \left[e^{\alpha(I_n - 1)^2} - 1 \right] \quad (6)$$

where fiber modulus ξ is greater than zero and exponential coefficient α is equal to or greater than zero.

In this constitutive model, six parameters (E , ν , θ , κ , ξ , and α) were used to describe the material behavior. For the compressible neo-Hookean ground substance, Young's Modulus E describes the stiffness and Poisson's ratio ν describes the Poisson effect. For the anisotropic fibrous network, preferential direction θ and concentration factor κ describe the fiber distribution, fiber modulus ξ describes the fiber stiffness, and α describes a single fiber's exponential behavior. E , ν , and ξ were determined by IFEA optimization (Sec. 2.8); θ and κ were determined by OCT and von Mises fitting ("Optical Coherence Tomography" and "Fiber Distribution Characterization" section); and α was chosen to be 5.7 based on our sensitivity study (Sec. 2.10).

Inverse Finite Element Analysis (IFEA)

We used an inverse finite element method, deploying a previously-verified genetic algorithm (GA) written in MATLAB, to fit model parameters to our experimental data.⁵⁰ Force-displacement and the equilibrium principal strain data of the specimen at the ROI were collected from the universal testing machine and DIC analysis results, respectively, as experimental (EXP) data. The same type of data was also collected from the corresponding region of the computational model as finite element (FEA) data (Figs. 4(c) and 4(d)). Three material parameters (E , ν , and ξ) were iteratively optimized within the boundaries listed in Table 3, and the following objective function was calculated and examined to find the best-fit material parameters,

$$\Xi(E, \nu, \xi) = \sum_{i=1}^N \left| \frac{e_1^{FEA^i} - e_1^{EXP^i}}{e_{norm}^{EXP^N}} \right| + \sum_{i=1}^N \left| \frac{e_2^{FEA^i} - e_2^{EXP^i}}{e_{norm}^{EXP^N}} \right| + \sum_{i=1}^N \left| \frac{F^{FEA^i} - F^{EXP^i}}{F^{EXP^N}} \right| \quad (7)$$

TABLE 3. IFEA fitted fiber composite material parameters.

Parameter	Mean value	Standard deviation
E [0.1, 100] kPa	1.758 kPa	0.670 kPa
ν [0, 0.499]	0.329	0.121
ξ [0.1, 10] kPa	0.389 kPa	0.341 kPa

Results represent all specimens including NP ($N = 14$) and PG ($N = 13$); Values in square brackets represent the search space of each parameter for IFEA based on preliminary results prior to IFEA and our previous study.⁵⁰

where i is the level number of the indentation test protocol with a total being $N = 4$, e represents the equilibrium principal strain of the specimen in the ROI, and F represents the equilibrium force of the indenter. The term e_{norm}^{EXP} is the Euclidean norm of e_1^{EXP} and e_2^{EXP} . Superscripts “FEA” and “EXP” denote the data of the finite element model and the experiment, respectively.

As a comparison and to provide a more simplistic modeling approach, we also performed IFEA on the indentation tests using a simple neo-Hookean model with model parameters E_{nH} and ν_{nH} . Optimization computations were run on Columbia University’s high-performance computer Terremoto (<https://cuit.columbia.edu/shared-research-computing-facility>).

Model Validation

Next, we validated the material model and best-fit material parameters against the measured 2-D strain field just outside the IFEA ROI. Error between the model and experiment just outside our ROI was calculated (comparing e_1^{FEA} and e_2^{FEA} to e_1^{EXP} and e_2^{EXP} , respectively). The resolution of the DIC experimental data was larger than the number of elements in the FEA model, so the DIC data were downsampled by averaging pixels falling within a fixed width of each FEA element. Natural neighbor interpolation algorithm in MATLAB was applied to fill vacancies in DIC results caused by imperfect speckle patterns. The error for each element of FEA was then calculated using

$$error = \left| \frac{e^{FEA} - e^{EXP}}{e^{EXP}} \right|. \quad (8)$$

To examine the fitness of our material model in tension, we applied the best-fit fiber composite models of six randomly-selected specimens (3 NP & 3 PG) to their tensile counterparts. We also applied a simple neo-Hookean model to them. We then used forward FEA to predict their stretches and stress responses under tension and compared the predictions with our tensile experimental results. For the uniaxial tensile experiments, we performed a three-level load–hold–

unload protocol on the same specimens from the indentation in a PBS bath on the universal testing machine. Two orthogonal cameras captured the specimen’s dimension changes from the front and the side. Tension displacements were prescribed as percentages of the grip-to-grip distance—15, 30, and 45%. The tissue was held for 30, 45, and 60 minutes to equilibrate after each displacement, respectively. Force–time (N·s) data were recorded using the material tester software (Instron, Inc., Blue Hill version 3.11.1209), and camera images were segmented in MATLAB to extract specimens’ dimensions.

Sample Topology Study and IFEA Sensitivity Study

We dissected the tissue using a customized slicer to create an even specimen surface. Hence, in an effort to quantitatively determine whether the tissue is sufficiently smooth, we performed a topology study using nano-indentation (Piuma, probe No.P190689, stiffness 0.49 N/m, tip radius 104 μm , Optics11 Life, Amsterdam) on one NP and one PG slice, both randomly chosen. On each slice, we tested two square areas with an edge length of 6 mm, equivalent to the maximum contact area during the indentation test. Within each area, we tested 49 spots in a 7×7 mesh grid, and the two areas were 5 mm apart. We then constructed three FEA models where the specimen had undulations (as tall as the largest detected height difference) on its top surface to simulate the unevenness, and the indenter tip was placed on top, in the valley, and on the ridge of the undulations. The indenter force and the first and second principal strains centered at the specimen bottom were compared between the scenarios.

Our previous study found the indentation test is not sensitive to changes in α ; we therefore set α to be 5.7 to reduce the unknown parameter set, improving accuracy.⁵⁰ α will be better informed by our ongoing tension study. To assess the sensitivity of all IFEA-fitted material parameters to the indentation test, we performed a sensitivity study on one NP and one PG specimen, both randomly chosen. We altered each of the three parameters, one at a time, from 10% to 200% of its best-fit value, and compared the differences in indenter force, and first and second principal strains. A new fitting error was also calculated using Eq. 7.

Statistical Analysis

One-way analysis of variance (ANOVA) was performed in MATLAB and R (a p -value of 0.05 was considered statistically significant) on the fiber distribution concentration factor (κ) and the IFEA-optimized material model parameter set (E , ν , and ξ) in several different comparison groups. These groups

were determined according to (1) the pregnancy status of the patient (non-pregnant, pregnant), (2) the anatomical locations of the specimen (anterior, posterior, fundus), and (3) the relative specimen depth in the uterine wall (outermost layer, middle layers, innermost layer).

RESULTS

Fiber Distribution

Preferential alignment of collagen fiber bundles is observed in the human uterine specimens collected for this study, evidenced by OCT and tissue strain data. Within the interrogated ROIs, one or two fiber families are found. Fig. 5 shows a representative fiber distribution characterization. For this specific NP fundus specimen, two von-Mises distributions ($\theta_1 = 0.49, \kappa_1 = 6.03; \theta_2 = 2.28, \kappa_2 = 2.11$) are fitted after 100 iterations. Among all 27 specimens, 36 von Mises distributions are fitted to 36 detected fiber families (Fig. 6(a)).

Both NP and PG uterine tissue samples contained preferentially-aligned fiber bundles, with significant differences in uterine fiber distribution (Fig. 6(a)). Each fiber family is represented by a single line in the figure, and the concentration of the fibers about the preferential direction, according to the von Mises distribution, is indicated by the color bar. Blue denotes a fiber concentration factor equal to zero, representing a uniform distribution, while red denotes a concentration factor equal to four, representing a more aligned distribution. Values larger than four ($N = 4$) are set

equal to four to improve presentation. The distribution concentration factors are compared between the NP and PG specimens quantitatively (Fig. 6(b)), and PG specimens have significantly smaller values ($p = 0.00362$), indicating a more uniform (dispersed) distribution. For the anterior and posterior specimens, the majority of NP fiber families orient at around $\pi/4$ and $3\pi/4$ (anatomically oblique), while the PG fiber families orient dominantly at $\pi/2$ (anatomically longitudinal) (Figs. 6(c) and 6(d)).

Indentation Test Force–Strain Response

Human uterine tissue displays a force–relaxation response to the ramp–hold displacement profile of the indentation test (Fig. 7(a)), and both the force and strain responses at equilibrium states are nonlinear with respect to the indenter displacements (Fig. 4). Among all fourteen NP specimen slices, the equilibrium force response distribution at the fourth level, 60% thickness displacement, is $0.051 \pm 0.023 N$. For thirteen PG specimen slices, the equilibrium force response distribution at the fourth level is $0.040 \pm 0.019 N$. Note, specimens have varying thicknesses due to tissue collection constraints. For almost all of the specimens, the principal strains (e_1^{EXP} and e_2^{EXP}) are at the maximum centered under the indenter (Figs. 7(b) and 7(c)), except for three PG specimens. (For these three specimens, it appears maximum strain may not have been centered under the indenter because indentation was performed at the boundary of two distinct fiber family profiles. In this case, the typical engineering assumption of affine motion of fibers with

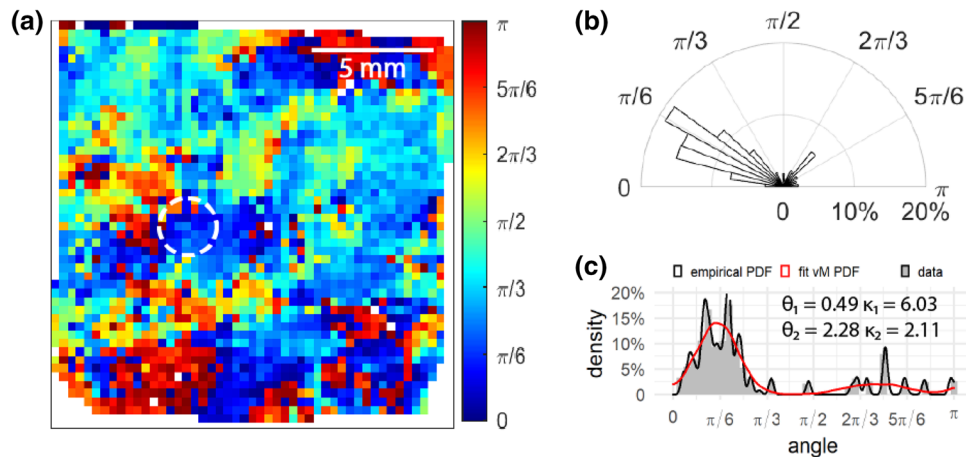


FIGURE 5. *En-face* θ data map fiber orientations, and a mixture of two von Mises distributions are fitted to the θ in the ROI. (a) θ data are obtained by the gradient-based method at each subset of one NP uterine slice. The fiber orientations in radian range from 0 to π . The white dashed-line circle denotes the ROI, a 2-mm circle centered under the indenter. White pixels on the specimen edge represent the background, while white pixels inside the specimen represent missing data from OCT. (b) A polar histogram for values of θ in the ROI was plotted from 0 to π , the resolution is $\pi/20$. (c) Histogram, empirical PDF, and fitted von Mises distribution of θ data in the ROI are plotted as the grey bars, the black line, and the red line, respectively. The values of θ and κ show the direction and concentration of the von Mises.

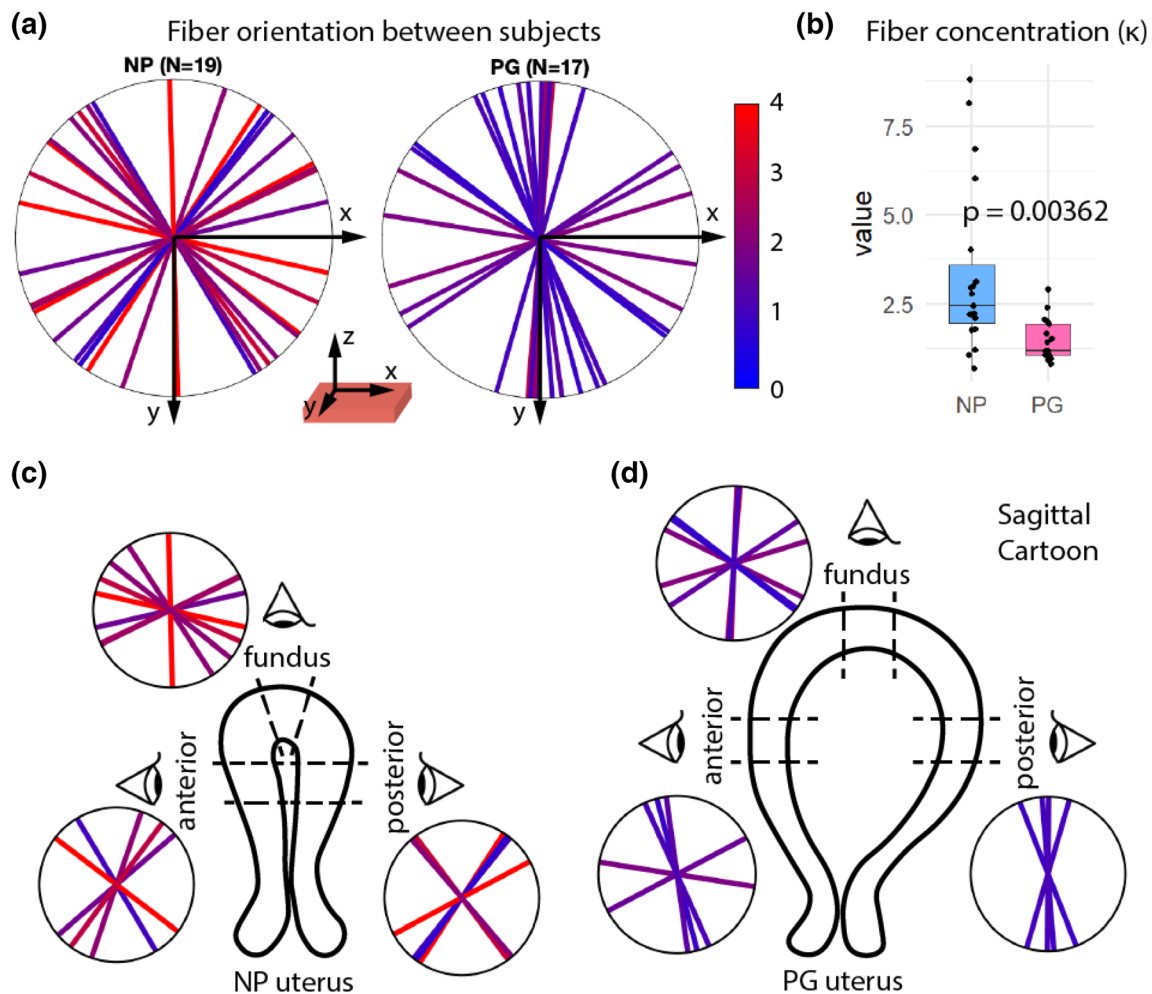


FIGURE 6. The fiber distribution compared between the NP and PG patients. (a) Each line represents one fiber family with its direction representing the preferred fiber orientation and its color representing the distribution concentration. The color bar denotes the value of the concentration factor with red equal to four (more concentrated) and blue equal to zero (uniformly distributed). The tissue is viewed from above. (b) Fiber concentration factors of the PG tissue are significantly ($p = 0.00362$) smaller than those of the NP tissue. (c)–(d) Fiber distributions viewed at various anatomical locations show NP tissue has more obliquely arranged fiber families; PG uterine tissue has more longitudinally arranged fiber families.

respect to the total deformation gradient does not hold.) Among all specimens, a large difference is observed between the first (e_1) and second (e_2) principal strain. The average of the ratios between these two strains of all specimens is 1.92 ± 0.72 . Therefore, this result indicates an anisotropy of various degrees in the uterine tissue's material properties. All specimen geometries and equilibrium force and strain data are available at the Columbia University Libraries' Academic Commons (<https://doi.org/10.7916/d8-r7mq-at21>).

IFEA: Best-Fit Material Parameters

Among IFEA-fitted parameters (E , ν , and ξ), E , and ν are found to be sensitive to the indentation test. This

is supported by large changes in indenter force and principal strains caused by changes in the parameter from our sensitivity study results (not detailed here). The best-fit parameter set for the fiber composite material model is averaged and listed in Table 3. Values in the table reflect the average of all data, including 27 indentation tests (four to six layers of the uterine wall at three anatomical locations of two human uteri) (Fig. 8). The GA-based optimization converged for all specimens. The errors calculated by the objective function (Eq. 7) $\Xi = 0.50 \pm 0.19$, indicating a nice fit by the defined criteria. The comparison of Young's modulus E and Poisson's ratio ν of the ground substance between the two patients show a discernible difference, although the high p -values suggest these differences are not significant. The average

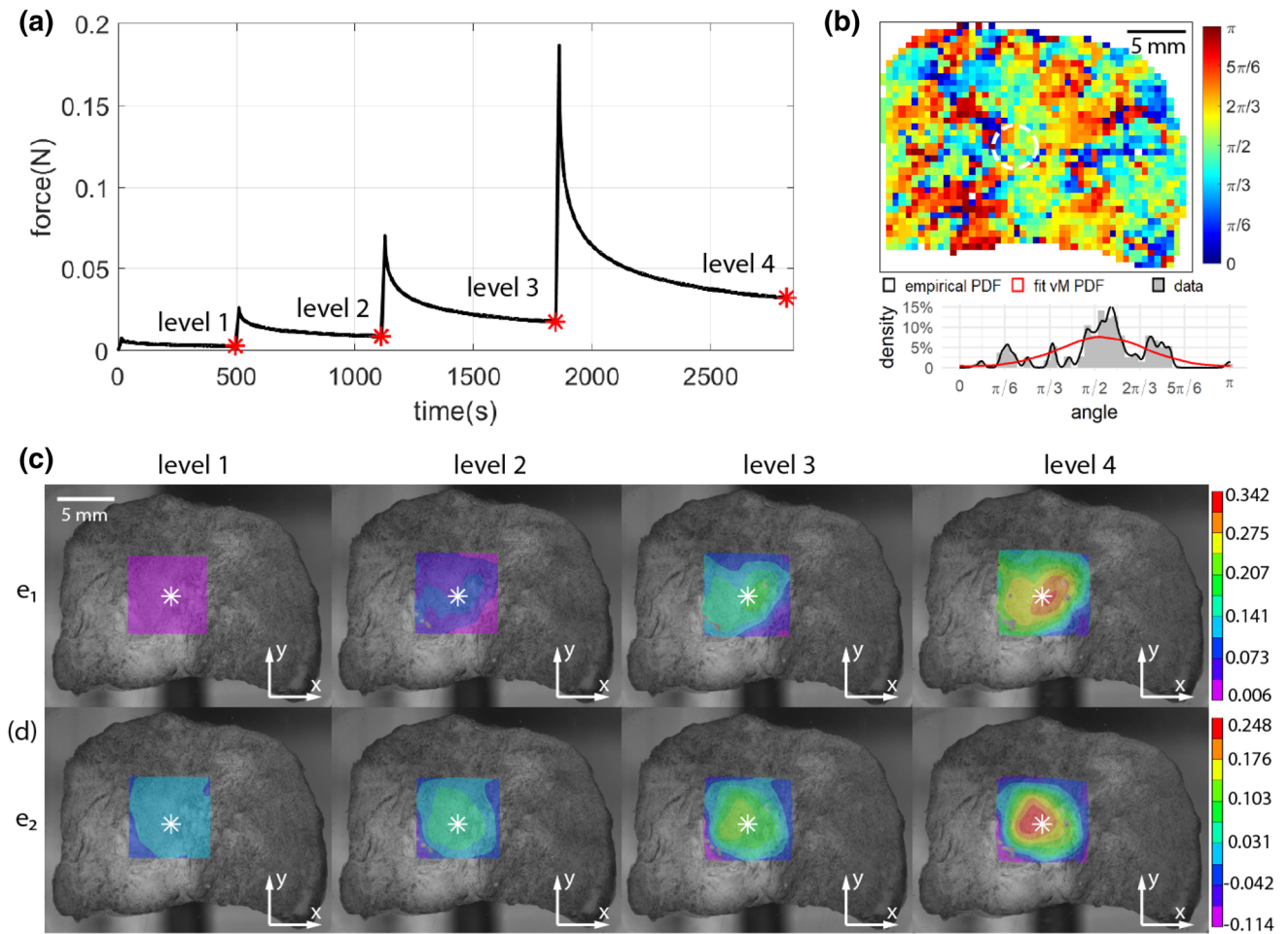


FIGURE 7. Force response of one PG fundus specimen and corresponding equilibrium principal strains at the four levels. (a) The black line represents the force response recorded by the Instron with red asterisks marking the equilibrium points at each level. (b) A von Mises distribution ($\mu = 1.65$, $\kappa = 2.13$) is fitted to the θ data in the ROI (white dashed-line circle) and plotted. (c)–(d) The DIC analysis renders the equilibrium first (e_1) and second (e_2) principal strain fields of the specimen bottom at each level with the white asterisks marking the indenting location. For each measurement (e_1 and e_2), the strain fields at different levels are in the same color scale.

of E is 1.758 kPa with a standard deviation of 0.670 kPa. The average of ν is 0.329 with a standard deviation of 0.121. The ξ are within the range of 0.1 to 1.339 kPa, and the average is 0.389 kPa with a standard deviation of 0.341 kPa.

The specimen bottom's first and second principal strain responses are found to be sensitive to ν and the fiber distribution (θ and κ) and are captured well by the anisotropic material model with a similar pattern and magnitude between the experiment and FEA (Fig. 9).

The best-fit parameter set (E_{nH} and ν_{nH}) for an isotropic neo-Hookean model is also listed (Table 4). The isotropic neo-Hookean material model is able to capture the force-displacement indentation response but does not capture the difference between the first and second principal strain.

Mapping Uterine Material Properties

Human uterine tissue displays heterogeneous mechanical properties at different anatomical locations and across different layers through the uterine wall (Fig. 10); an intrasubject analysis accounts for incomparable uterine pathology (more details are included in “Discussion” section). Fourteen NP specimens in total were tested from the anterior ($n = 4$), the fundus ($n = 5$), and the posterior ($n = 5$) of the uterus (Fig. 10(a)). At each location, the total number of uterine slices differs due to differing uterine wall thicknesses (Fig. 10(b)). Noncontinuous numbers indicate certain slices were not mechanically tested due to the histology process where specimens were fixed and embedded in paraffin blocks, and therefore, un-

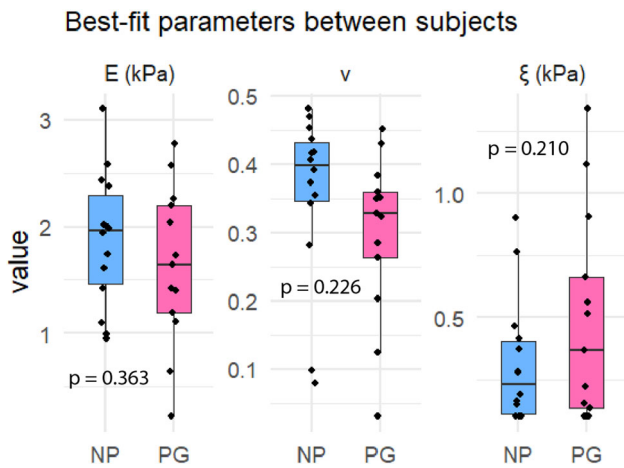


FIGURE 8. The best-fit material parameters are compared between the NP and PG tissue. The average E and average ν of the NP tissue are both slightly larger than those of the PG tissue, while the ξ has a reversed trend. However, the high p -values evaluated by one-way ANOVA in R suggest these differences are not significant.

able to be mechanically tested. Young's modulus E appears to be significantly different between NP anatomical locations ($p = 0.0229$). Poisson's ratio ν of the NP posterior specimens has a wide spread of values where the middle three layers are much larger than the innermost and outermost layers. Thirteen PG specimens in total were tested from the anterior ($n = 4$), the fundus ($n = 4$), and the posterior ($n = 5$) of the uterus (Fig. 10(c)). Poisson's ratio ν of the PG posterior specimens has a wide spread of values. No significant differences are observed otherwise, as suggested by high p -values. However, due to the difficulty of collecting specimens from human subjects, the sample size of this study is small, limiting its statistical significance.

DISCUSSION

In this study, the anisotropic material behavior of two human uteri is characterized at various anatomical locations using spherical indentation coupled with 2-dimensional video extensometry. We improve on previous methods by (1) developing a new fiber distribution characterization method using the imaging results to reveal uterine tissue anisotropy and (2) employing the observed fiber structure to optimize material modeling. Using a non-destructive imaging modality, OCT, instrumented spherical indentation, and inverse finite element analysis, the anisotropic mechanical properties of two human uteri are discovered, compared, and reported.

Previous Mechanical Characterization of Human Uterine Tissue

Human uterine tissue has been tested in multiple mechanical loading conditions, both *ex vivo* and *in vivo*. A study compared the passive stress–relaxation response of non-pregnant (NP) and pregnant (PG) uteri from 92 patients using tensile tests.⁸ The study found the NP tissue exhibits a steeper stress–strain response, indicating a higher elastic modulus, than the PG response. One of the first studies to combine tension and compression tests on the human uterus found a nonlinear relationship between true stress and true strain, which agrees with our findings. The study reports the Young's modulus under compression ranges from 68.95 to 103.42 kPa.⁴⁶ Our best-fit isotropic neo-Hookean Young's modulus E_{nH} ranges from 0.35 to 3.99 kPa. These results differ by two orders of magnitude from Pearsall *et al.* because we analyze equilibrium rather than instantaneous tissue behavior. A nonlinear stress–strain relationship was also observed in a study quantifying uterine dynamic material properties (strain rate $1.5 s^{-1}$) under tension.³⁶ Almost all PG uterine strips broke at a similar peak strain (0.32 ± 0.112), exhibiting a peak stress of $656 \pm 484 kPa$. Anisotropic material properties were observed in human uterine tissue using strain gauge rosette and aspiration tests, both *ex vivo* and *in vivo*.^{28,39} The former discovered the anisotropic behavior of the uterine muscle progresses with stages of labor at the anterior and fundal regions, while the latter test collected different stretch values at the ventral, dorsal, and fundal uterine regions under the same aspiration pressure.

Fiber Distribution Characterization

Both non-pregnant (NP) and pregnant (PG) tissue have anisotropic material properties, but there is a significant difference in uterine fiber distribution between the two. Various fiber orientations ranging from 0 to π are observed among all specimens from two uteri (Fig. 6(a)). Among NP specimens, the majority of fiber families orient at around $\pi/4$ and $3\pi/4$ (Fig. 6(c)), indicating an obliquely arranged architecture consistent with a previous study.⁶⁰ This feature also agrees with our previous findings in a fiber tractography study using OCT, in which two almost-orthogonal fiber tracts can be seen weaving with each other between planes.³⁸ Among PG specimens, more fiber families orient at around $\pi/2$ (Fig. 6(d)), indicating a more longitudinally or meridionally arranged architecture. Additionally, fiber families of PG tissue display a significantly lower degree of concentration, indicating a more dispersed distribution around the

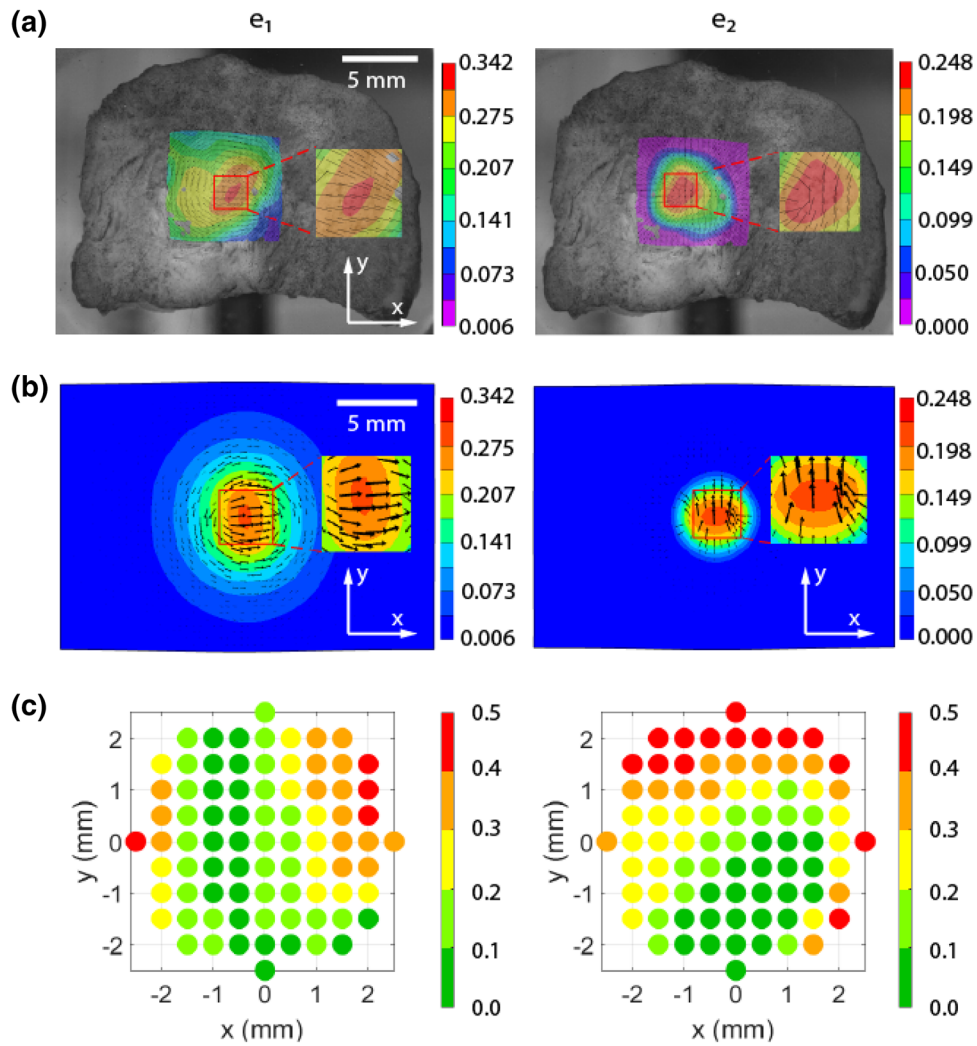


FIGURE 9. Comparison of the first (e_1) and second (e_2) principal strain fields between the experiment and FEA. (a) The experimental data e_1^{EXP} and e_2^{EXP} are plotted with the color bar indicating the magnitude. The red-square areas are viewed close up to show the vector directions indicated by the lines. (b) The corresponding FEA data e_1^{FEA} and e_2^{FEA} are plotted with the arrows indicating the vector directions. (c) Error maps of a 5-mm diameter circle around the indenter (0, 0) are generated between the strain fields of the experiment and FEA (Sec. 2.9). Errors larger than 0.5 are set equal to 0.5 for a more refined representation. Data are from one PG fundus specimen.

TABLE 4. IFEA fitted neo-Hookean material parameters.

Parameter	Mean value	Standard deviation
E_{nH} [0.1, 100] kPa	2.180 kPa	0.834 kPa
ν_{nH} [0, 0.499]	0.258	0.141

Results represent all specimens including NP ($N = 14$) and PG ($N = 13$); Values in square brackets represent the search space of each parameter for IFEA based on preliminary results prior to IFEA and our previous study.⁵⁰

preferential orientation. During pregnancy, the uterus grows upward and develops out of the pelvic region starting week 12, and by week 36, the top of the uterus is at the tip of the xiphoid cartilage at the lower end of the breastbone. Therefore, it makes sense to find more

fibers longitudinally aligned to bear strain caused by an almost 6-fold length increase.¹⁹ While the fiber families orient more longitudinally, they also become more dispersed to accommodate a change in uterine size along other directions.

Material Behavior of Human Uterine Tissue

The force response of human uterine tissue to spherical indentation is time-dependent and nonlinear (Fig. 4(d)), and uterine fiber architecture dictates the 2-D principal strain fields (Fig. 9(a)–(b)), similar to human cervical tissue.⁵⁰ A time-dependent behavior of the human uterus is observed with force–relaxation to a hold in displacement (Fig. 3(e)). Future work will

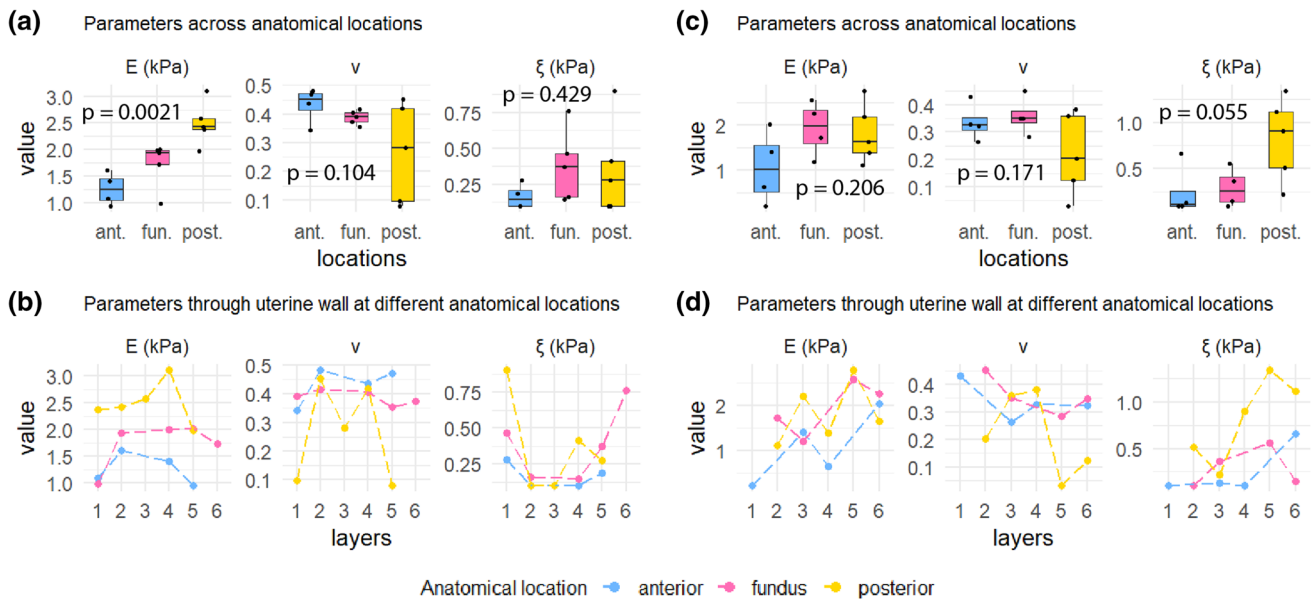


FIGURE 10. The fitted parameters of the NP and PG uteri compared across anatomical locations and through the uterine wall thickness within each subject. (a)–(b): NP; (c)–(d): PG; ant.: anterior; fun.: fundus; post.: posterior; 1: the outermost layer; 6: the innermost layer. (a) The posterior NP uterine tissue has the largest E , followed by the fundus and the anterior. The difference of ν and ξ at different locations are not significant. (b) For the NP tissue, E is larger at the middle layers while fiber stiffness is smaller at the middle layers when compared to the innermost and outermost layers. ν is larger at the middle layers for posterior uterine tissue but similar throughout the layers for anterior and fundus tissue. (c) For the PG tissue, all three parameters are similar at different locations. (d) ν is larger at the outer layers for anterior and fundus tissue of the PG uterus.

address this time-dependent material behavior of uterine tissue because the evolution of the time-dependent behavior is a key characteristic of tissue remodeling in pregnancy.⁶³ To lay the foundation for possible visco- and/or poroelastic mechanisms in the uterus, this study focuses on developing an equilibrium material model first. Focusing at the ROI, the first and second principal strain fields differ significantly from each other, indicating an anisotropic fiber distribution. The first principal strain e_1 runs perpendicular to tissue fibers while the second principal strain e_2 runs parallel to tissue fibers. For instance, in the presented specimen (Fig. 9), the observed distribution of fibers in the ROI is a von Mises with $\mu = 85.631$ ($\approx \pi/2$) and $\kappa = 1.017$. This angle is perpendicular to the first principal strain field and parallel to the second principal strain field observed in the experiments (Fig. 9(a)). The ratio between the first and second principal strain is approximately 1.44, which is relatively small among all specimens. This ratio is consistent with its $\kappa = 1.017$ being relatively small among all specimens, as a smaller concentration factor represents a more uniform fiber distribution that contributes to a more uniform strain distribution. Therefore, we have found uterine fiber distribution contributes mechanically to uterine material response to indentation loading.

Overall, the Young's modulus of the ground substance E is 1.756 ± 0.685 kPa for the equilibrium

response, smaller than cervical tissue (3.20 ± 3.30 kPa) but in the same order of magnitude. The Poisson's ratio of the ground substance ν is 0.329 ± 0.124 , which is higher than cervical tissue (0.22 ± 0.13), indicating the uterus has a lower level of compressibility.⁵⁰ Though the differences between subjects are not statistically significant, this may be attributable to the pathological nature of these specimens (Table 1). For the NP uterus, the reported cause for hysterectomy was severe fibroids (in particular, the uterus was anteverted and enlarged to the size of a 20-week pregnant uterus). Fibroids, also known as leiomyoma, are muscular tumors that grow in the uterine wall and can cause abdominal pain, heavy menstrual bleeding, and pressure on surrounding organs. A study on 19 fibroids from 8 women has shown wide-spanned stiffness measurements ($3.028 - 14.18$ kPa) by rheometry among all subjects and a within-subject coefficient of variation ranging from 1.6 to 42.9%,²⁶ suggesting that fibroids behave differently from nonpathological uterine tissue. Despite an effort to avoid visible fibroids during tissue collection, its severe pathology means that small fibroids were difficult to completely avoid. For the PG uterus, the reported cause for Cesarean hysterectomy is complete previa and posterior placenta accreta. Complete previa refers to the condition where the placenta overlies the cervix's internal os, blocking the pathway for the fetus during delivery. Placenta

accreta refers to the condition where the placenta invades the myometrium and cannot safely detach from the uterine wall during delivery. Though it is still unclear why these placenta abnormalities happen, scarring caused by the Cesarean incision is suspected as the primary cause.⁴⁵ A previous study using shear wave velocity to investigate placenta function has found placentas with abnormal location (placenta previa), and penetration (placenta accreta) has higher shear wave velocity than the placenta of normal pregnancy.²³ It is possible for the inner layers of the collected posterior uterine tissue to be mixed with placental tissue, thus affecting the measured material responses.

Within the NP uterus, significant differences ($p = 0.0021$) are observed in Young's modulus E between anatomical locations. The posterior tissue has the highest value, followed by the fundus and the anterior. The Poisson's ratio ν appears to have a reverse trend, but it is not significant due to the wide range of posterior measurements. There is no difference observed in fiber stiffness ξ . Through uterine wall layers, both E and ν seem to have higher values in the middle layers while having lower values for the outermost and innermost layers. This trend is reversed for the measurements of ξ . Biologically, the NP uterine wall consists of three distinct layers (perimetrium, myometrium, and endometrium, from outermost to innermost). Different layers perform specific functions to maintain healthy menstruation and to prepare for a potential pregnancy. Therefore, it makes sense for them to exhibit different material properties. Perimetrium is the outer serosa layer that is very thin and can be identified as approximately half the thickness of the slices numbered as 1. However, the exact thickness of the endometrium varies between subjects and points in time during a menstrual cycle. Thus, we cannot conclusively identify whether the remaining slices come from the myometrium or endometrium. Once pregnant, the most inner layer, the endometrium, transitions into the decidua as part of the placenta to provide support and protection for gestation. Therefore, all of the PG specimens except slices numbered "1" can be identified as myometrium. Within the PG uterus, posterior inner layers have significantly smaller ν and larger ξ compared to the rest of the tissue, which could be due to the previously discussed placenta penetration condition.

The spherical indentation method presented in this work imposes a complex stress field in the tissue and features a wide range of compressive and tensile strains (0.36 ± 0.15 —average maximum first principal strain; -0.37 ± 0.03 —average maximum compressive third principal strain; both informed by FEA). When applied to the tensile loading condition, the fiber-composite material model captures the tissue stretch

ratios well (Fig. 11(d) and 11(h)). Our predictions for the tissue's Cauchy stress, however, exhibit mixed performance. Between the two cases reported here, one is able to capture the tensile stress response up to a Lagrangian strain level of 0.54 and exhibits an obvious superiority over a simple neo-Hookean model for capturing nonlinearities (Fig. 11(c)), while the other prediction diverts from the experimental result at 0.22 Lagrangian strain and exhibits a similar linearity as a neo-Hookean model (Fig. 11(g)). Hence, the anisotropic material properties reported in this work (Table 3) can be applied to loading conditions that fall between -0.30 to 0.22 Lagrangian strain and if the magnitude and pattern of tissue strain drive a critical biologic mechanism, as in cellular responses in mechanobiology.²¹ Otherwise, if the pattern of strain in the tissue is not important, then the isotropic neo-Hookean material model and properties (Table 4) can be used to describe the uterine tissue in the small strain regime. The presented fiber composite model is also able to capture the tissue's anisotropic material behavior informed by different fiber distributions, where fibers in ROI 1 orient dominantly parallel to the tensile direction, while the orientation is perpendicular in ROI 2 (Fig. 11(f)). This makes sense as fibers are shown to be stiffer in the direction of their alignment.^{20,29,31,61}

Experimental and Computational Error Analysis

Experimental errors are introduced by the load cell tolerance (0.005 N), the displacement resolution (8 μm), and the buoyancy force ($F_b < \rho g V < 0.001$ N) exerted on the indenter. Errors are also introduced into the force–displacement response by the specimen topology. Our topology study results show the largest height difference within each area is between 0.25 and 0.5 mm. The first and second principal strains of the specimen bottom and the indenter forces between the three scenarios where the indenter is placed at different locations of the uneven surface all differ less than 2%. When mapping the indenter location onto the OCT image for the fiber distribution characterization, errors are introduced by the small distortion of the specimen caused by the freeze–thaw cycle between the OCT scanning and the mechanical testing. To reduce this error impact, we matched the northwestern and southeastern corners of the specimen in one image on top of the corners in the other image when manually overlaying the OCT camera image and the indentation camera image. For errors introduced by the DIC process, they are treated in the same way as our previous study, as well as the GA-based optimization.⁵⁰ For the finite element modeling process, the errors are introduced by fixing the far-end side surface com-

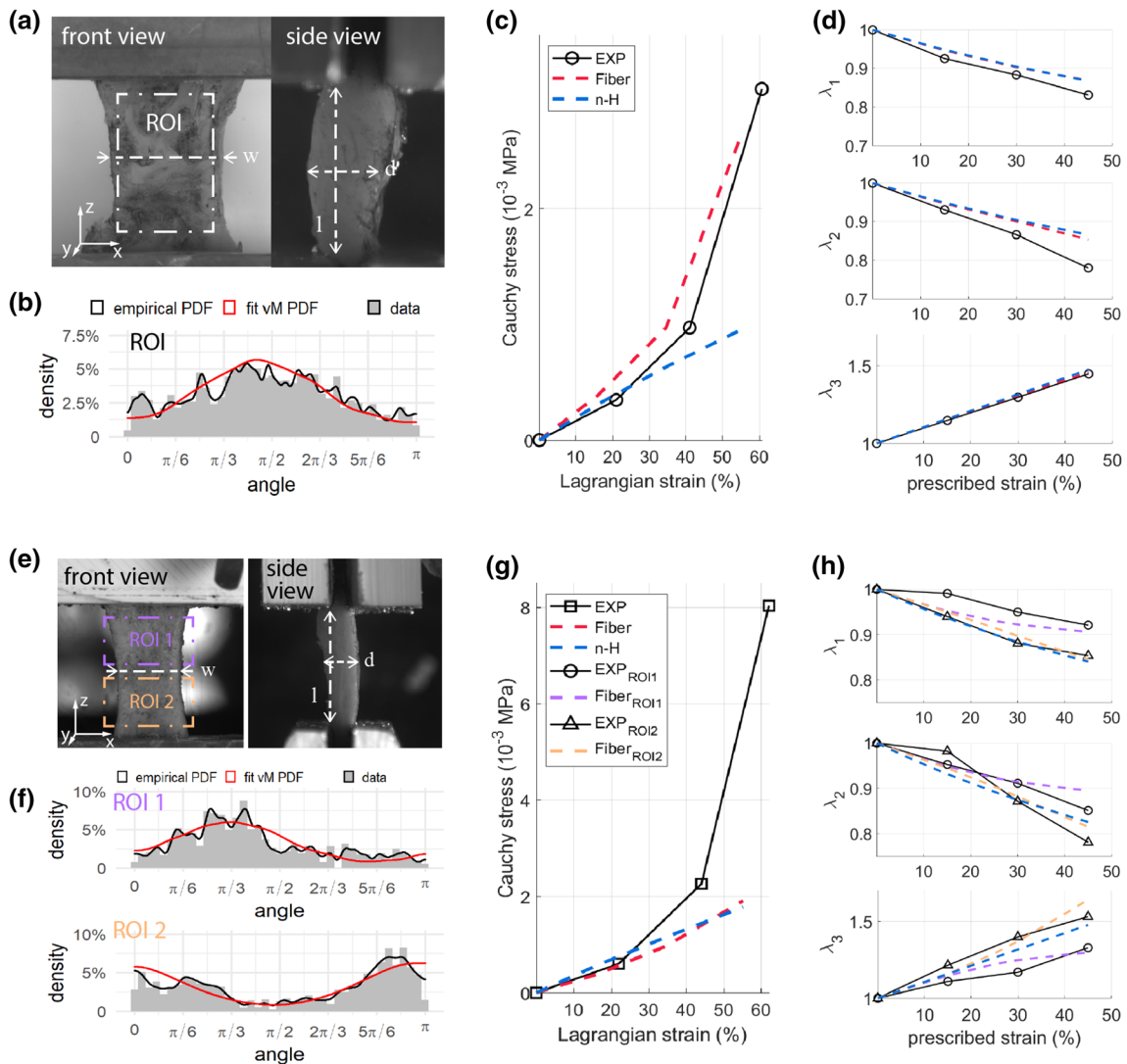


FIGURE 11. Comparisons between the best-fit model predictions and experimental results under tension. (a)–(d): one NP fundus specimen; (e)–(h): one NP posterior specimen; both specimens are randomly selected for validation. (a) and (e) Camera images of the specimen in the tensile test. The width (w) of the specimen is measured from the front, while the depth (d) and length (l) are measured from the side. The second specimen is divided into two ROIs based on its fiber distribution characterized using the method in “Fiber Distribution Characterization” section. (b) and (f) von Mises distributions are fitted to the fibers in the ROIs. The angle is measured relative to the positive x -axis. (c) and (g) Cauchy stress–Lagrangian strain curves of the experiment, our fibrous model, and the neo-Hookean model are represented by the markers, the red, and the blue dashed line, respectively. (d) and (h) The stretch ratios of the width (λ_1), depth (λ_2), and length (λ_3) are compared between the experiment (markers), the fibrous model, and the neo-Hookean model (colored dashed lines).

pletely to stabilize the geometry. To assess the impact of this boundary assignment, we conducted a comparative FEA test on five randomly selected specimen models by instead fixing the nearer orthogonal side surface. Results showed the same strain field pattern and a less than 2% difference in magnitude and a less than 3% difference in force change, indicating the impact caused by fixing the boundary is negligible.

Limitations

While the IFEA and indentation test capture the material behavior of human uterine tissue well among 27 specimen slices, the material model fits for two specimens demonstrate a subjectively large error. For these cases, the strains of the specimen bottom surface are not well predicted due to its uneven surface and imperfect speckle quality, both contributing to the complex deformation pattern recorded by DIC for the strain analysis.

Our validation study shows the fitted material model predicts the principal strains effectively within the 4-mm diameter circle around the indenter, as shown by small errors, but less accurately outside this circle, as shown by larger errors (Fig. 9(c)). This is expected for the following reasons: first, the stress distribution is more nonuniform further away from the ROI; second, fiber distribution outside this region varies significantly and is not encompassed for characterization and IFEA (Fig. 12). A parallel computational study is underway to implement the characterized fiber distribution into the FEA at the scale of the whole specimen. Future work will also develop a mechanical test that provides a uniform stress field to characterize the material property across the whole specimen.

Due to the nature of the tissue collection process and restrictions we faced in the operating room, our specimens went through two freeze–thaw cycles in total, from tissue collection to OCT scanning and mechanical testing. Many previous studies on soft tissue with similar components have found mixed results on whether and how freeze–thaw cycles affect the tissue’s mechanical properties.^{1,11} We previously performed comparison mechanical tests on a different set of PG uterine tissue (16 C-section uteri) when they were fresh (≤ 2 hours after surgery) and thawed (at 4 °C for 12 hours, from -80 °C for more than 24 hours). No systematic stiffening or weakening due to freeze–thaw was observed.

Our sensitivity studies (not shown here) on uterine tissue (and previously on cervical tissue⁵⁰) have concluded the fiber stiffness ξ affects tensile response more than it affects compressive response, which is largely due to the fiber recruitment process of collagenous tissue under different loadings.^{22,42,55,57} Therefore, it is not sensitive to the indentation loading. A parallel

study using tensile tests coupled with IFEA is underway to better capture the fiber stiffness value.

With the current state of knowledge, we treated the SMC-collagen fibrous network the same way as collagen fibers alone, as we do not have further data to understand how SMCs and collagen fibers within the uterine tissue separate from or interact with each other. This assumption may be an important oversimplification and further studies are warranted.

Finally, this study is a case study on two specific uteri under compressive loads. For obvious reasons, specimens collected from hysterectomy are usually pathological. The NP and PG uteri are from an African-American and a white patient, respectively. Differences in uterine material properties between women of different racial backgrounds have been demonstrated elsewhere,^{6,37} but these differences are not explored in this study. During pregnancy, more complex loading patterns, such as abrupt fetal movement or an acute external impact, may occur and are not studied in this work. Biological tissue has different material behaviors under differing loading conditions.^{16,40,43,56} Therefore, the reported material properties should only be applied to similar strain regimes and study objectives as advised in “Material Behavior of Human Uterine Tissue” section.

Conclusions

Human uterine tissue has anisotropic material properties, which facilitates its complex biomechanical function in pregnancy. This study provides mechanical testing data and an initial 3-D anisotropic constitutive modeling framework that incorporates quantitative tissue fiber architecture. Mechanical data are presented for a non-pregnant and pregnant uterus at various anatomical locations and through-thickness locations

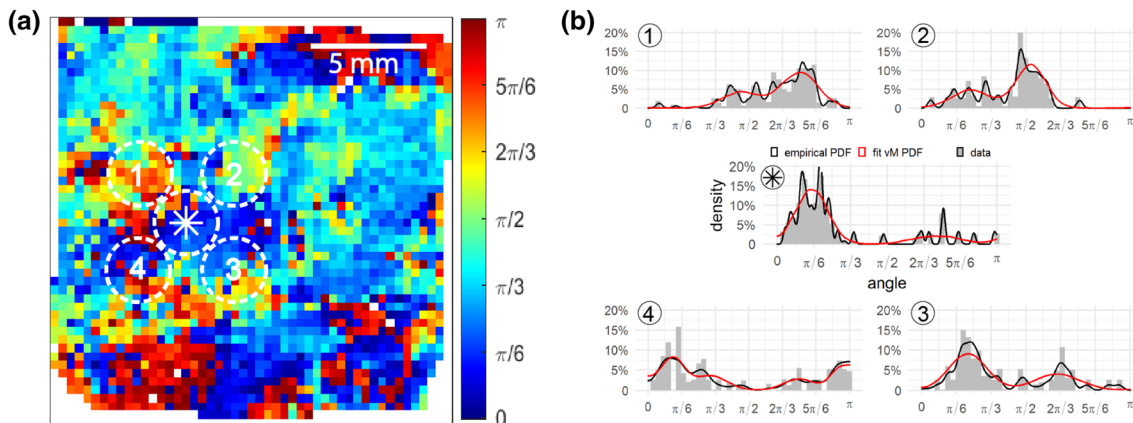


FIGURE 12. Fiber distributions exhibit spatial variations. (a) Four 4-mm diameter circles are selected in the close vicinity of the ROI, and their θ data are collected. (b) Histograms and fittings of the θ of the four circles show spatial variations between the regions. The numbers (1–4) denote the correspondence between the circles and their θ fittings, and the asterisk represents the indenter location. All x-axes are the angle of fiber orientation, and all y-axes are the frequency density.

using spherical indentation coupled with video extensometry. Although difficult to analyze given complex stress distributions, spherical indentation allows for material property mapping, preserves tissue architecture, and enables follow-up tensile testing of the tissue sample. Aided by finite element analysis, the constitutive model's material parameters are optimized to describe the specimen's indentation response and 2-D strain field against its rigid substrate. The model captures the tissue's material response, where the inclusion of the oriented fiber solid network allows for an accurate description of tissue strain. There is no significant difference in material stiffness parameters between the non-pregnant and pregnant specimens studied here, although the pregnant tissue has a more dispersed fiber distribution. Both non-pregnant and pregnant samples have heterogeneous material properties. The specimens are taken from patients with known pathology. Hence, this study serves as a first step to establish a viable mechanical testing framework that accounts for the nonlinear and anisotropic material properties of the human uterus.

ACKNOWLEDGMENTS

The authors would like to thank Andrew Wilson from the Columbia University Department of International and Public Affairs for contributing to optimize the von Mises fitting algorithm, Dr. Arnold Advincula and Dr. Fady Collado from the Columbia University Irving Medical Center Department of Obstetrics and Gynecology for the uterine tissue specimen collection, and Dr. George Gallos from the Columbia University Irving Medical Center Department of Anesthesiology for teaching us the exquisite function of the uterus. Research reported in this publication was supported by the Eunice Kennedy Shriver National Institute Of Child Health & Human Development under Award Number R01HD091153 and R01HD072077 to KMM. The content is solely the responsibility of the authors and does not necessarily represent the official views of the National Institutes of Health.

REFERENCES

¹Adham, M., J.-P. Gournier, J.-P. Favre, E. De La Roche, C. Ducerf, J. Baulieux, X. Barral, and M. Pouyet. Mechanical characteristics of fresh and frozen human descending thoracic aorta. *J. Surg. Res.* 64:32–34, 1996.

- ²Agostino, R. B. D., A. Belanger, and R. B. D. Agostino. A suggestion for using powerful and informative tests of normality. *Commentaries* 44:316–321, 1990.
- ³Al-Zirqi, I., B. Stray-Pedersen, L. Forsén, and S. Vangen. Uterine rupture after previous caesarean section: uterine rupture. *BJOG* 117:809–820, 2010.
- ⁴Allisoon R. Gillies, R. L. L. Structure and function of the skeletal muscle extracellular matrix. *Muscle Nerve* 44:318–331, 2011.
- ⁵Ambrosi, C. M., V. V. Fedorov, I. R. Efimov, R. B. Schuessler, and A. M. Rollins. Quantification of fiber orientation in the canine atrial pacemaker complex using optical coherence tomography. *J. Biomed. Opt.* 17:1, 2012.
- ⁶Catherino, W., H. Eltoukhi, and A. Al-Hendy. Racial and ethnic differences in the pathogenesis and clinical manifestations of uterine leiomyoma. *Semin. Reprod. Med.* 31:370–379, 2013.
- ⁷Chakraborty, S. and S. W. K. Wong. BAMB: An R package for Fitting Bivariate Angular Mixture Models. [arXiv:1708.07804](https://arxiv.org/abs/1708.07804) [stat], 2019. [ArXiv: 1708.07804](https://arxiv.org/abs/1708.07804).
- ⁸Conrad, J. T., W. L. Johnson, W. K. Kuhn, and C. A. Hunter Jr. Passive stretch relationships in human uterine muscle. *Am. J. Obstet. Gynecol.* 96:1055–1059, 1966.
- ⁹Cook, J. L., D. B. Zaragoza, D. H. Sung, and D. M. Olson. Expression of myometrial activation and stimulation genes in a mouse model of preterm labor: myometrial activation, stimulation, and preterm labor. *Endocrinology* 141:1718–1728, 2000.
- ¹⁰Delaine-Smith, R., S. Burney, F. Balkwill, and M. Knight. Experimental validation of a flat punch indentation methodology calibrated against unconfined compression tests for determination of soft tissue biomechanics. *J. Mech. Behav. Biomed. Mater.* 60:401–415, 2016.
- ¹¹Delgadillo, J., S. Delorme, R. El-Ayoubi, R. Diraddo, and S. Hatzikiriakos. Effect of freezing on the passive mechanical properties of arterial samples. *J. Biomed. Sci. Eng.* 337088:645–652, 2010.
- ¹²Fernandez, M., M. House, S. Jambawalikar, N. Zork, J. Vink, R. Wapner, and K. Myers. Investigating the mechanical function of the cervix during pregnancy using finite element models derived from high-resolution 3D MRI. *Comput. Methods Biomech. Biomed. Eng.* 19:404–417, 2016.
- ¹³Fleming, C. P., C. M. Ripplinger, B. Webb, I. R. Efimov, and A. M. Rollins. Quantification of cardiac fiber orientation using optical coherence tomography. *J. Biomed. Opt.* 13:030505, 2008.
- ¹⁴Fonda, J. Ultrasound diagnosis of caesarean scar defects. *Australas. J. Ultrasound Med.* 14:22–30, 2011.
- ¹⁵Foot, N. C. The Masson trichrome staining methods in routine laboratory use. *Stain Technol.* 8:101–110, 1933.
- ¹⁶Fung, Y.-c. *Biomechanics: Mechanical Properties of Living Tissues*. New York: Springer, 2013.
- ¹⁷Gan, Y., W. Yao, K. M. Myers, J. Y. Vink, R. J. Wapner, and C. P. Hendon. Analyzing three-dimensional ultrastructure of human cervical tissue using optical coherence tomography. *Biomed. Opt. Express* 6:1090–1108, 2015.
- ¹⁸Gasser, T. C., R. W. Ogden, and G. A. Holzapfel. Hyperelastic modelling of arterial layers with distributed collagen fibre orientations. *J. R. So. Interface* 3:15–35, 2006.
- ¹⁹Gillespie, E. C. Principles of uterine growth in pregnancy. *Am J Obstet Gynecol* 59:949–959, 1950.
- ²⁰Girton, T. S., V. H. Barocas, and R. T. Tranquillo. Confined compression of a tissue-equivalent: collagen fibril and

- cell alignment in response to Anisotropic Strain.*J. Biomech. Eng.* 124:568–575, 2002.
- ²¹Hall, M. S., F. Alisafaei, E. Ban, X. Feng, C. Y. Hui, V. B. Shenoy, and M. Wu. Fibrous nonlinear elasticity enables positive mechanical feedback between cells and ECMs.*Proc. Natl. Acad. Sci. U.S.A.* 113:14043–14048, 2016.
- ²²Hansen, K. A., J. A. Weiss, and J. K. Barton. Recruitment of tendon crimp with applied tensile strain.*J. Biomech. Eng.* 124:72–77, 2002.
- ²³Hefeda, M. M. and A. Zakaria. Shear wave velocity by quantitative acoustic radiation force impulse in the placenta of normal and high-risk pregnancy.*Egypt. J. Radiol. Nucl. Med.* 51, 2020.
- ²⁴Holzappel, G. A., T. C. Gasser, and R. W. Ogden. A new constitutive framework for arterial wall mechanics and a comparative study of material models.*J. Elast. Phys. Sci. Solids* 61:1–48, 2000.
- ²⁵Holzappel, G. A., R. W. Ogden, and S. Sherifova. On fibre dispersion modelling of soft biological tissues: a review.*Proc. R. Soc. A* 475: 20180736, 2019.
- ²⁶Jayes, F. L., B. Liu, L. Feng, N. Aviles-Espinoza, S. Leikin, and P. C. Leppert. Evidence of biomechanical and collagen heterogeneity in uterine fibroids.*PLoS ONE* 14:e0215646, 2019.
- ²⁷Jayyosi, C., N. Lee, and S. Nallasamy. Swelling behavior of the pregnant mouse cervix in physiological and hyperosmotic solutions. In: 8th World Congress of Biomechanics, pp. 8–12. 2018.
- ²⁸Kauer, M., V. Vuskovic, J. Dual, G. Szekely, and M. Bajka. Inverse finite element characterization of soft tissues. Lecture Notes in Computer Science (including subseries Lecture Notes in Artificial Intelligence and Lecture Notes in Bioinformatics) 2208:128–136, 2001. ISBN: 3540426973.
- ²⁹Komai, Y. and T. Ushikif. The three-dimensional organization of collagen fibrils in the human cornea and sclera.*Invest. Ophthalmol. Vis. Sci.* 32: 2244–2258, 1991.
- ³⁰Krouskop, T. A., T. M. Wheeler, F. Kallel, B. S. Garra, and T. Hall. Elastic moduli of breast and prostate tissues under compression.*Ultrason. Imaging* 20:260–274, 1998.
- ³¹Lake, S. P. and V. H. Barocas. Mechanics and kinematics of soft tissue under indentation are determined by the degree of initial collagen fiber alignment.*J. Mech. Behav. Biomed. Mater.* 13:25–35, 2012.
- ³²Lee, S. W., J. Y. Yoo, J. H. Kang, M. S. Kang, S. H. Jung, Y. S. Chong, D. S. Cha, K. H. Han, H. Y. Choi, and B. M. Kim. Diagnosis of cervical intraepithelial neoplasm (CIN) using polarization-sensitive optical coherence tomography. Optics InfoBase Conference Papers 16:2709–2719, 2007. ISBN: 1424411742.
- ³³Liu, L., S. Oza, D. Hogan, Y. Chu, J. Perin, J. Zhu, J. E. Lawn, S. Cousens, C. Mathers, and R. E. Black. Global, regional, and national causes of under-5 mortality in 2000–15: an updated systematic analysis with implications for the sustainable development goals.*Lancet* 388:3027–3035, 2016.
- ³⁴Lye, T. H., C. C. Marboe, and C. P. Hendon. Imaging of subendocardial adipose tissue and fiber orientation distributions in the human left atrium using optical coherence tomography.*J. Cardiovasc. Electrophysiol.* 30:2950–2959, 2019.
- ³⁵Mak, A., W. Lai, and V. Mow. Biphasic indentation of articular cartilage—I. Theoretical analysis.*J. Biomech.* 20:703–714, 1987.
- ³⁶Manoogian, S. J., J. A. Bisplinghoff, A. R. Kemper, and S. M. Duma. Dynamic material properties of the pregnant human uterus.*J. Biomech.* 45:1724–1727, 2012.
- ³⁷Marsh, E. E., G. E. Ekpo, E. R. Cardozo, M. Brocks, T. Dune, and L. S. Cohen. Racial differences in fibroid prevalence and ultrasound findings in asymptomatic young women (18–30 years old): a pilot study.*Fertil. Steril.* 99:1951–1957, 2013.
- ³⁸McLean, J., S. Fang, G. Gallos, K. Myers, and C. Hendon. 3-D collagen fiber mapping and tractography of human uterine tissue using OCT.*Biomed. Opt. Express* 11:5518–5541, 2020.
- ³⁹Mizrahi, J., Z. Karni, and W. Z. Polishuk. Isotropy and anisotropy of uterine muscle during labor contraction.*J. Biomech.* 13:211–218, 1980.
- ⁴⁰Myers, E. R. and V. C. Mow. Biomechanics of cartilage and its response to biomechanical stimuli. In *Cartilage: Structure, Function, and Biochemistry* pp. 313–341, 1983.
- ⁴¹Myers, K. M. and D. Elad. Biomechanics of the human uterus. Wiley Interdisciplinary Reviews. Systems Biology and Medicine 9, 2017.
- ⁴²Myers, K. M., S. Socrate, A. Paskaleva, and M. House. A study of the anisotropy and tension/compression behavior of human cervical tissue.*J. Biomech. Eng.* 132, 2010.
- ⁴³Nordin, M. and V. H. Frankel. Basic Biomechanics of the Musculoskeletal System. Philadelphia: Lippincott Williams & Wilkins, 2001.
- ⁴⁴Orfanoudaki, I. M., D. Kappou, and S. Sifakis. Recent advances in optical imaging for cervical cancer detection.*Arch. Gynecol. Obstet.* 284:1197–1208, 2011.
- ⁴⁵Oyelese, Y. and J. C. Smulian. Placenta previa, placenta accreta, and vasa previa.*Obstet. Gynecol.* 108:694, 2006.
- ⁴⁶Pearsall, G. W. and V. L. Roberts. Passive mechanical properties of uterine muscle (myometrium) tested in vitro.*J. Biomech.* 11:167–176, 1978.
- ⁴⁷Pino, J. H. Arrangement of muscle fibers in the myometrium of the human uterus: a mesoscopic study.*MOJ Anat. Physiol.* 4:280–283, 2017.
- ⁴⁸Purslow, P. P. and J. A. Trotter. The morphology and mechanical properties of endomysium in series-fibred muscles: variations with muscle length.*J. Muscle Res. Cell Motil.* 15:299–308, 1994.
- ⁴⁹Rashid, B., M. Destrade, and M. D. Gilchrist. Determination of friction coefficient in unconfined compression of brain tissue.*J. Mech. Behav. Biomed. Mater.* 14:163–171, 2012.
- ⁵⁰Shi, L., W. Yao, Y. Gan, L. Y. Zhao, W. Eugene McKee, J. Vink, R. J. Wapner, C. P. Hendon, and K. Myers. Anisotropic material characterization of human cervix tissue based on indentation and inverse finite element analysis.*J. Biomech. Eng.* 141, 2019.
- ⁵¹Smith, R., M. Imtiaz, D. Banney, J. W. Paul, and R. C. Young. Why the heart is like an orchestra and the uterus is like a soccer crowd. *American Journal of Obstetrics and Gynecology* 213:181–185, 2015. Amsterdam: Elsevier.
- ⁵²Solutions, C. Vic-2D v6. VIC-3D 2010 Reference Manual, p. 108, 2010.
- ⁵³Sutton, M. A., J. J. Orteu, and H. Schreier. Image Correlation for Shape, Motion and Deformation Measurements: Basic Concepts, Theory and Applications. Springer, 2009.
- ⁵⁴Tadepalli, S. C., A. Erdemir, and P. R. Cavanagh. Comparison of hexahedral and tetrahedral elements in finite element analysis of the foot and footwear.*J. Biomech.* 44:2337–2343, 2011.

- ⁵⁵Tan, T. and R. De Vita. A structural constitutive model for smooth muscle contraction in biological tissues. *Int. J. Non-Linear Mech.* 75:46–53, 2015.
- ⁵⁶Tanaka, E. and T. van Eijden. Biomechanical behavior of the temporomandibular joint disc. *Crit. Rev. Oral Biol.* 14:138–150, 2003.
- ⁵⁷Thornton, G. M., C. B. Frank, and N. G. Shrive. Ligament creep behavior can be predicted from stress relaxation by incorporating fiber recruitment. *J. Rheol.* 45:493–507, 2001.
- ⁵⁸Trotter, J. A. and P. P. Purslow. Functional morphology of the endomysium in series fibered muscles. *J. Morphol.* 212:109–122, 1992.
- ⁵⁹Wang, Y., S. Son, S. M. Swartz, and N. C. Goulbourne. A mixed von mises distribution for modeling soft biological tissues with two distributed fiber properties. *Int. J. Solids Struct.* 49:2914–2923, 2012.
- ⁶⁰Weiss, S., T. Jaermann, P. Schmid, P. Staempfli, P. Boesiger, P. Niederer, R. Caduff, and M. Bajka. Three-dimensional fiber architecture of the nonpregnant human uterus determined *ex vivo* using magnetic resonance diffusion tensor imaging. *Anat. Rec. Part A* 288:84–90, 2006.
- ⁶¹Xu, B., M.-J. Chow, and Y. Zhang. Experimental and modeling study of collagen scaffolds with the effects of crosslinking and fiber alignment. *Int. J. Biomater.* 2011, 2011.
- ⁶²Yao, W., Y. Gan, K. M. Myers, J. Y. Vink, R. J. Wapner, and C. P. Hendon. Collagen fiber orientation and dispersion in the upper cervix of non-pregnant and pregnant women. *PLoS ONE* 11:1–20, 2016.
- ⁶³Yoshida, K., C. Jayyosi, N. Lee, M. Mahendroo, and K. M. Myers. Mechanics of cervical remodelling: insights from rodent models of pregnancy. *Interface Focus* 9:20190026, 2019.
- ⁶⁴Zhai, L., M. L. Palmeri, R. R. Bouchard, R. W. Nightingale, and K. R. Nightingale. An integrated indenter-arfi imaging system for tissue stiffness quantification. *Ultrasonic Imaging* 30:95–111, 2008.

Publisher's Note Springer Nature remains neutral with regard to jurisdictional claims in published maps and institutional affiliations.